JOURNAL OF APPLIED PHYSICS **103**, 114503 (2008)

Bandstructure effects in ultra-thin-body double-gate field effect transistor: A fullband analysis

Kausik Majumdar[a] and Navakanta Bhat[b]
Department of Electrical Communication Engineering, Indian Institute of Science, Bangalore-560012, India

(Received 12 February 2008; accepted 29 March 2008; published online 5 June 2008)

The properties of an *n*-channel ultra-thin-body (UTB) double-gate field effect transistor (DGFET), resulting from the bandstructure of the thin film Si channel, are discussed in this paper. The bandstructure has been calculated using a ten-orbital $sp^3d^5s^*$ tight-binding method. A number of intrinsic properties including band gap, density of states, intrinsic carrier concentration, and parabolic effective mass have been derived from the calculated bandstructure. The spatial distributions of intrinsic carrier concentration and ⟨100⟩ effective mass, resulting from the wave functions of different contributing subbands, are analyzed. A self-consistent solution of coupled Poisson-Schrödinger equations is obtained taking the full bandstructure into account, which is then applied to analyze volume inversion. The spatial distribution of carriers over the channel of a DGFET has been calculated and its effect on effective mass and channel capacitance is discussed.

[DOI: 10.1063/1.2937186]

I. INTRODUCTION

The interest in ultra-thin-body (UTB) double-gate field effect transistor (DGFET) has grown in the recent past because of its superior properties compared to bulk FET. DGFET is being considered as one of the promising future alternatives to replace the present day bulk devices.[1,2] The intrinsic quantum confinement provided by its unique geometric structure, coupled with better gate control from both top and bottom, affects the characteristics of UTB DGFET.[3] The different aspects of classical modeling of DGFETs have been discussed in Refs. 4–6. There are a number of reports on the quantum mechanical effects on DGFET, both analytical as well as numerical.[3,7–9] For numerical analysis, one has to solve coupled Poisson-Schrödinger equations self-consistently.[10] This is done either by assuming some analytical $E-\bar{k}$ relationship or by taking the full bandstructure into account. There has been a considerable amount of work on calculation of the bandstructure of materials,[11–17] which can be plugged into the self-consistent Poisson-Schrödinger equations.[18]

DGFET has a unique property called "volume inversion," which improves the transport characteristics enormously.[1,3] This can be explained with the help of quantum effects. Another important aspect is a substantial change in transport properties depending on the crystallographic orientation,[19–21] which can be analyzed from the detailed bandstructure calculation. Gradual thinning of the channel region decreases the intrinsic carrier concentration, leading to interesting effects on the total channel capacitance of DGFET.[22–24]

The aim of this paper is to focus on the detailed analysis of some of the key effects in UTB-DGFET, which arise entirely because of the bandstructure of the channel material and are not very apparent. Only silicon has been considered as the thin channel material in this work, but this can be easily extended to other channel materials as well. The fullband structure calculation used here is based on $sp^3d^5s^*$ tight-binding method.[14–16] The calculated bandstructure has then been used to predict some intrinsic properties of thin film Si including band gap, density of states, intrinsic carrier concentration, and effective mass. Interesting deviations in different characteristics are observed in ultra-thin film silicon when compared to bulk silicon. Following this, the Poisson-Schrödinger coupled equations are solved self-consistently taking care of the full bandstructure. This is used to critically analyze the volume inversion phenomenon, thereby providing new physical insights. This, in turn, throws some light on the spatial distribution of the carriers inside the DGFET channel. Taking this into account, the total channel capacitance and the evolution of effective mass from the source end to the drain end along the channel have been analyzed.

The rest of the paper is organized as follows: Sec. II describes the details of the $sp^3d^5s^*$ tight-binding method of bandstructure calculation for an ultra-thin film. The different intrinsic transport properties of ultra-thin film silicon have been discussed in Sec. III. Poisson-Schrödinger coupled equations have been solved self-consistently and related analysis has been performed in Sec. IV. Finally, the paper is concluded in Sec. V.

II. BANDSTRUCTURE CALCULATION

The tight-binding method of bandstructure calculation has been studied extensively by many researchers.[11–17] In this work, a ten-orbital $sp^3d^5s^*$ tight-binding method[14–16] has been used to find the bandstructure of the thin film of silicon. Only the onsite energies and two-center overlap integrals of nearest neighbors have been taken into account. Spin orbit interaction has been neglected, and thus each $\bar{k}$ point in the Brillouin zone is assumed to be degenerate with two spin

---

[a] Author to whom correspondence should be addressed. Electronic mail: kausik@ece.iisc.ernet.in.

[b] Electronic mail: navakant@ece.iisc.ernet.in.

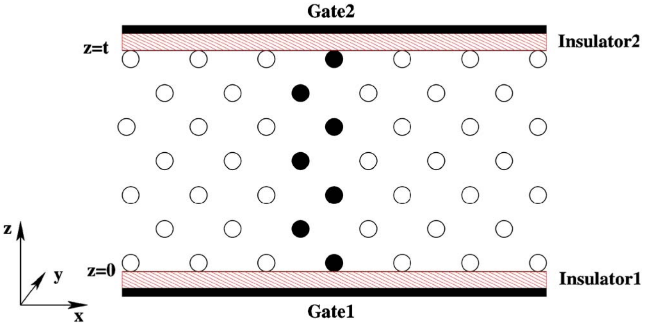

FIG. 1. (Color online) A 7 monolayer thick film with basis atoms (black dots). The basis atoms can be spanned in whole $2-D$ along x and y to construct the thin film.

states. Infinite crystal periodicity has been assumed along the channel length and width directions and thus Bloch's theorem is assumed to hold good in those directions. However, along the thickness of the channel, the crystal is truncated to a few monolayers of atoms and, thus, the crystal periodicity cannot be assumed in this direction. Suppose the thickness contains N atomic monolayers. Then, the truncated crystal can be formed by taking a basis of N atoms along the thickness direction and spanning them over the whole 2-D space. Figure 1 shows a 7 monolayer thick channel with the basis atoms shown as black dots. The channel region can be formed by spanning the basis atoms along x and y. The tight-binding fitting parameters for Si, used in this work, have been taken from Refs. 15 and 16. An N monolayer thick film will produce a $10N \times 10N$ tight-binding Hamiltonian matrix.[18] To get rid of the huge number of surface states (whose energy eigenvalues often fall inside the semiconductor band gap) caused by the dangling bonds, it has been assumed that the surfaces are completely passivated by hydrogen. This has been achieved by artificially increasing the onsite energies of the s and p orbitals of the surface atoms, as described in Ref. 17.

The assumption of this method is that the electronic wave function is strictly guided in the $x-y$ plane. Thus, the Brillouin zone comprises of a 2-D $\bar{k}$ space, as opposed to a 3-D one in the bulk case. k_z has been assumed to be zero throughout this paper. The whole $2-D$ Brillouin zone has been discretized using a step size of $0.05 \times (2\pi/a)$ for both k_x and k_y, where a is the lattice constant (=5.43 Å for Si). In this paper, the film thickness has been referenced to the number of monolayers (AL) in the film. An N AL thick Si film translates to a thickness of $a(N-1)/4$. Figure 2 shows the energy dispersion plot of a 17 monolayer thick ($\sim$2.17 nm) Si film over the whole 2-D Brillouin zone. Only the top-most valence subband and the bottom-most conduction subband have been included in Fig. 2 for clarity. Throughout this paper, the valleys occurring at Γ point and at $\sim 0.8(2\pi/a)$ along the X direction are termed as Γ valley and X valley, respectively.

III. INTRINSIC PROPERTIES OF THIN FILM SI

In this section, different intrinsic electrical properties of ultra-thin Si film have been derived from the calculated bandstructure.

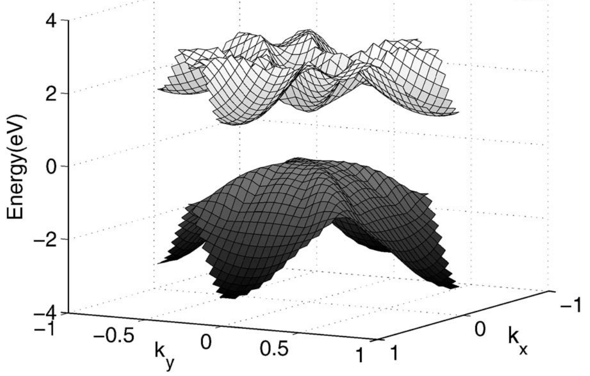

FIG. 2. $E-k$ relationship of top-most valence subband and bottom-most conduction subband over the whole $2-D$ Brillouin zone of a 17 monolayer thick Si film. The conduction band minimum occurs at Γ point. The X valley is fourfold degenerate.

A. Bandgap and density of states

It has been well established in literature, both theoretically as well as experimentally, that at the nano-scale, band gap of semiconductors is a function of the size of the material. As the size reduces, the band gap of the material increases. Figure 3 shows how the Γ gap and X gap of a Si film vary as a function of the film thickness. One should note that, for a sufficiently thin film, as opposed to the bulk case, the conduction band minimum occurs at direct Γ point and not in the X direction. Thus the electrons will first populate the Γ valley and, hence, one can expect to see drastic change in transport properties for a thin film Si channel compared to bulk. As the film thickness increases, the energy difference $\Delta E_{\Gamma X}$ between Γ and X valleys decreases, and electrons start populating the X valley as well. Finally, at sufficiently large film thickness, at the bulk limit, the X valley is of lower energy compared to the Γ valley. In Fig. 4, the 2-D density of states has been plotted as a function of electron energy in the conduction band, for four different film thickness values. In the calculation, the energy has been discretized in steps of 0.2 eV. Just above the cut-off energy (conduction band minimum), only the Γ valley contributes. However, as energy

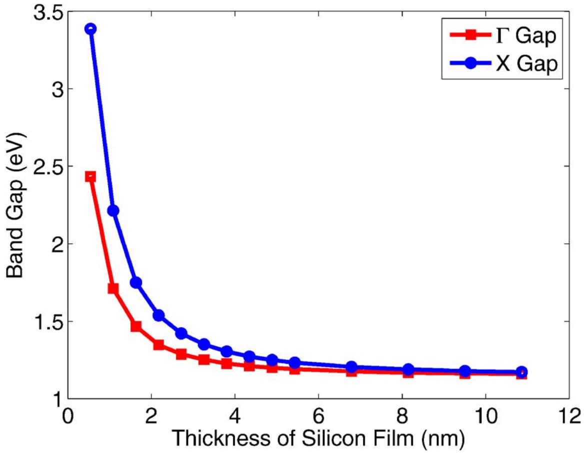

FIG. 3. (Color online) Calculated Γ and X gap of silicon thin film as a function of film thickness. For sufficiently small thickness, direct Γ gap is much larger compared to the next gap occurring at the X valley.

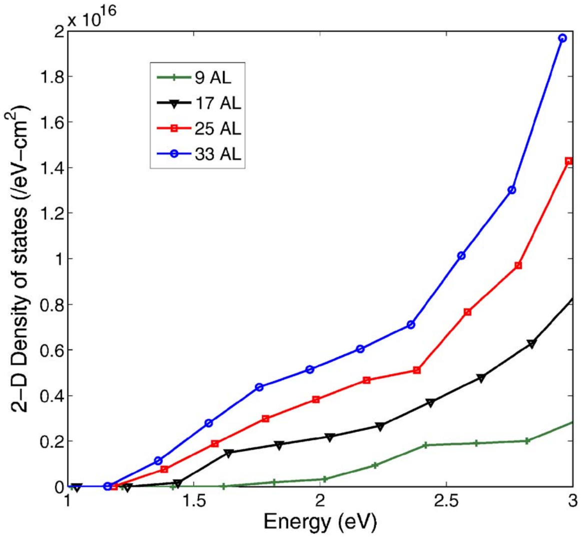

FIG. 4. (Color online) 2-D DOS as a function of electronic energy for different thickness values of the Si film. The energy space is discretized by steps of 0.2 eV.

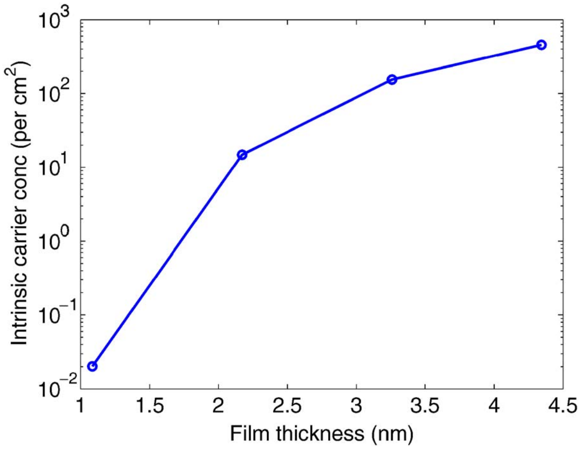

FIG. 5. (Color online) Intrinsic carrier concentration per unit area (i.e., total number of carriers contained in the film with unity area) as a function of Si film thickness.

increases, other regions of the Brillouin zone also start contributing. As expected, the density of states for thicker film is larger.

B. Intrinsic carrier concentration

Since the band gap increases at nano-scale, one expects lower intrinsic carrier concentration as the film thickness reduces. The per unit area intrinsic electron concentration at temperature T is given by

$$n_A = \sum_j \sum_{\bar{k}} 2f(E_j^{\bar{k}}), \tag{1}$$

where the first sum is over different subband indices j of the conduction band and the second sum is over different $\bar{k}$ points in the first Brillouin zone. $E_j^{\bar{k}}$ represents the energy eigenvalue at the $\bar{k}$th point of the jth subband index. The Fermi-Dirac probability $f(E_j^{\bar{k}})$ is given by

$$f(E_j^{\bar{k}}) = \frac{1}{1 + e^{(E_j^{\bar{k}} - \mu)/k_B T}}. \tag{2}$$

k_B is the Boltzmann constant and μ is the chemical potential. Figure 5 shows that the intrinsic carrier concentration per unit area decreases as the film thickness is reduced. However, apart from the reduction in carrier concentration, another important observation is that the carrier concentration has a distribution along the film thickness, which peaks at the center of the film. This is due to the spatial distribution of the wave functions of the electronic states contributing to the carrier concentration. If the film of thickness t has N monolayers, then the film can be assumed to be discretized by N points. The volume concentration of carriers at each of these points is given by

$$n^0(z) = \frac{N}{t} \sum_j \sum_{\bar{k}} 2f(E_j^{\bar{k}}) |\psi_j^{\bar{k}}(z)|^2, \tag{3}$$

where $\psi_j^{\bar{k}}(z)$ is the wave function of the electronic state $(j, \bar{k})$ at z. Figure 6 plots the fractional contribution of different subbands to the total electron concentration for a thin film of Si. Γ_i and X_j represent the ith subband of the Γ valley and the jth subband of the X valley, respectively. It is clear that, for very small thickness, only Γ_1 and Γ_2 subbands contribute, but as thickness increases, other subbands also start contributing. In Figs. 7 and 8, the spatial distribution of intrinsic carrier concentration, contributed from different subbands, has been shown for 9 and 33 monolayer thick Si films, respectively. Since for a 9 monolayer thick film ($\sim$1.086 nm) only Γ_1 and Γ_2 contribute, the spatial distribution of the total electron concentration is dictated by the wave functions of only these two subands. The peak concentration comes at the middle of the film and reduces as it approaches the surface. However, for a 33 monolayer thick film ($\sim$4.344 nm), four Γ subbands and the bottom most X

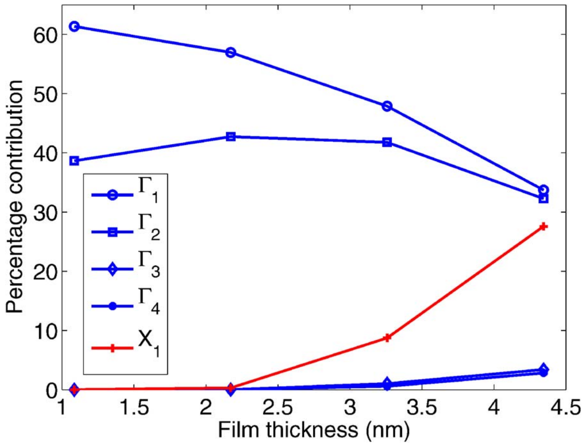

FIG. 6. (Color online) Percentage contribution to per unit area intrinsic carrier concentration from different Si subbands lying in Γ and X valleys. For very small thickness only Γ_1 and Γ_2 contribute, but at larger thickness, electrons start populating other valleys as well.

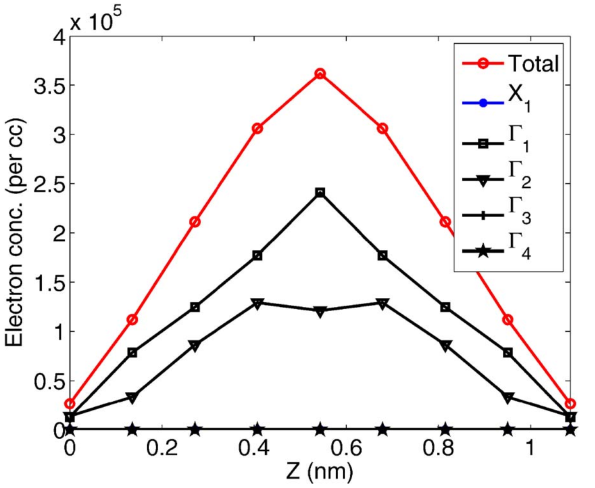

FIG. 7. (Color online) Carrier distribution along channel thickness of different subbands lying in Γ and X valleys for a 9 atomic layer thick Si film.

subband contribute, and this, in turn, affects the total carrier distribution, as shown in Fig. 8.

C. Parabolic effective mass and its validity

A simple parabolic effective mass has been derived in this section at the minima of different subbands to show some interesting transport properties of thin film. Parabolic effective mass $m^*(i,j)$ for the ith valley and jth subband is defined as

$$m^*(i,j) = \frac{\hbar^2}{\partial^2 E(i,j)/\partial \bar{k}^2(i,j)}. \tag{4}$$

The parabolic effective mass (m^*) has been calculated at the minima of the two bottom-most subbands Γ_1 and Γ_2 for four different film thickness values. It is plotted in Figs. 9 and 10 along different crystal directions after normalization with respect to the electron rest mass (m_0). It is observed that, in both cases, for 9 monolayer thick film, the effective mass is highly anisotropic. For Γ_1, the effective mass increases as one moves from [10] direction to [11] direction, whereas it

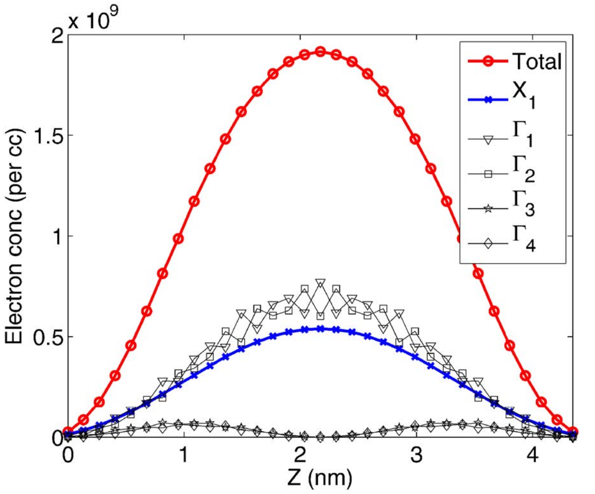

FIG. 8. (Color online) Carrier distribution along channel thickness of different subbands lying in Γ and X valleys for a 33 atomic layer thick Si film.

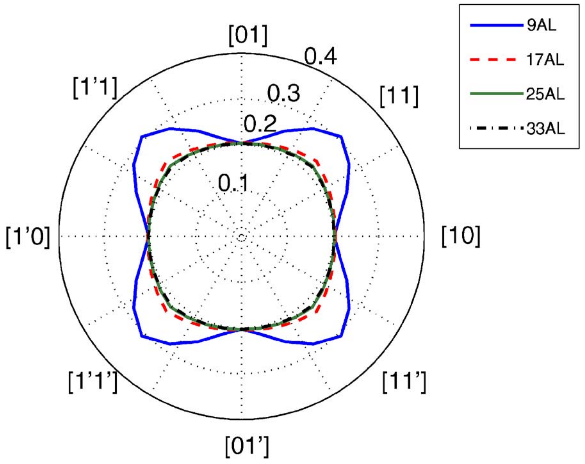

FIG. 9. (Color online) Variation of parabolic effective mass at the minimum of first Γ subband with crystal direction and Si film thickness. Anisotropy is observed at small film thickness.

reduces for the Γ_2 valley. However, for larger thickness, the effective mass in both the valleys becomes fairly isotropic. Since the effective mass varies with subbands, and the electron concentration in different subbands has different spatial distributions, it is expected that the effective mass should also have a spatial distribution. A "*distributed effective mass*," say $M^*(z)$, a function of the depth z along the thickness of the film, has been defined as

$$M^*(z) = \frac{1}{\sum_{i,j} \frac{W_{ij}(z)}{m^*(i,j)}}, \tag{5}$$

where $W_{ij}(z)$ represents the fractional contribution to the electron concentration at depth z from the jth subband of the ith valley. This way of defining $\langle 100\rangle$ $M^*(z)$ has the underlying assumption that all the electrons (more generally, an equal fraction of electrons from each subband of every valley) are moving along the $\langle 100\rangle$ direction. Figure 11 shows that for thinner films, $\langle 100\rangle$ $M^*(z)$ is more or less uniform (which is because all the electrons are in Γ_1 and Γ_2 subbands

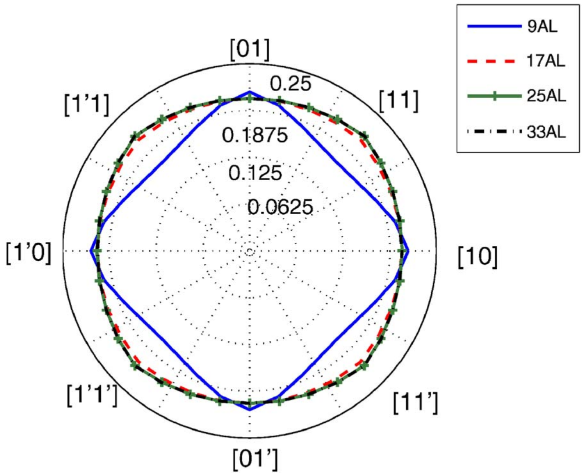

FIG. 10. (Color online) Variation of parabolic effective mass at the minimum of second Γ subband with crystal direction and Si film thickness. For very small thickness (~1 nm), $\langle 111\rangle$ effective mass is smaller than $\langle 100\rangle$ effective mass.

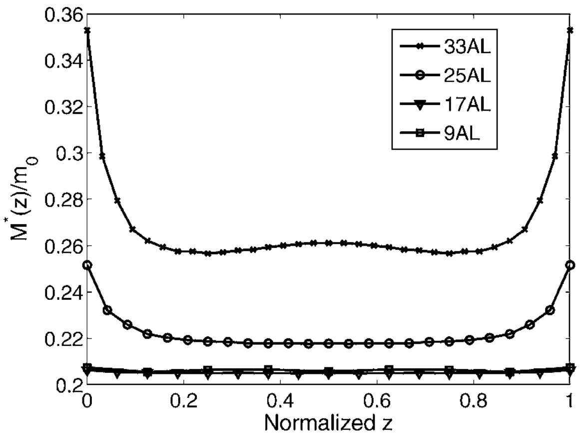

FIG. 11. Distribution of ⟨100⟩ $M^*(z)$ along film thickness for various values of Si film thickness. Increasing thickness increases $M^*(z)$ and reduces spatial uniformity.

possess almost the same ⟨100⟩ effective mass). However, with the increase in film thickness, $M^*(z)$ at positions closer to the surface becomes larger than that of the central part of the film. Thus, for larger film thickness, the carriers closer to the center of the film are expected to have higher mobility than those that are closer to the surface. This effect is inherent to the intrinsic film, arising from the spatial distribution of the wave functions associated with different subbands. Another interesting observation is that a 9 monolayer thick film has (marginally) larger ⟨100⟩ effective mass than a 17 monolayer thick film at all z. This is because of the fact that the Γ_2 valley has larger ⟨100⟩ effective mass for 9 monolayer thick film (Fig. 10).

However, one should note that parabolic effective mass approximation is valid only for electrons with smaller energy in the conduction band. The solid curves in Fig. 12 show the $E-\bar{k}$ relationship along the ⟨100⟩ direction for the four bottom-most conduction subbands, calculated from the tight-binding method, as described in Sec. II. The dotted curves show the fitted parabolic bands with same effective masses, as calculated from Eq. (4). ΔE_s represents the electronic energy range in the sth subband between which the parabolic $E-\bar{k}$ tracks the tight-binding $E-\bar{k}$ fairly well. From Fig. 12, it is clearly visible that parabolic bands fail to track the actual bands for electron energies in excess of ~0.5 eV, referenced from corresponding band minimum, in all the cases. Nevertheless, the above simple analysis gives a good qualitative insight about transport and mobility.

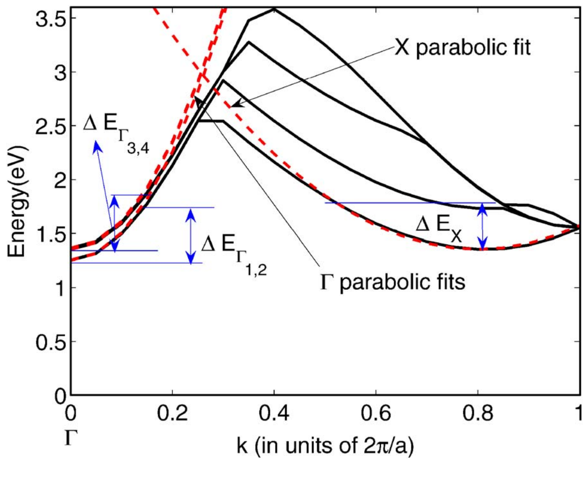

FIG. 12. (Color online) Original tight-binding bandstructure data and corresponding parabolic fits at four bottom-most Γ subbands and bottom-most X subband for ⟨100⟩ Si. The fits are reasonable for energy values less than ~0.5 eV referenced from corresponding subband minima.

IV. SELF-CONSISTENT SOLUTION OF COUPLED POISSON-SCHRÖDINGER EQUATIONS

To study the effect of gate voltage on this structure, a model device has been assumed which consists of a top gate and a bottom gate separated from the film by thin insulator layers, as shown in Fig. 1. The Si film is assumed to be undoped. Thus the channel charge corresponds to only mobile charge. If $\phi(z)$ is the potential at z, then one can write the 1-D Poisson equation as[4,10]

$$\frac{\partial^2\phi(z)}{\partial z^2} = \frac{qN}{\epsilon_0\epsilon_{rs}t}\Big[\sum_j\sum_{\bar{k}} 2f(E_j^{\bar{k}})|\psi_j^{\bar{k}}(\phi,z)|^2\Big]e^{(q\phi(z)/k_BT)}, \qquad (6)$$

where q is electronic charge, ϵ_0 is permittivity of vacuum, and ϵ_{rs} is the relative permittivity of the channel material. The boundary conditions are derived from the fact that the normal component of the displacement vectors inside Si and insulators will be the same at $z=0$ and $z=t$. Thus, at the boundaries, one can have

$$\epsilon_{rs}\frac{\partial\phi(z)}{\partial z}\bigg|_{z=0} = -\,\epsilon_{r1}\frac{V_{g1}-V_{fb1}-\phi(0)}{t_{ox1}} \qquad (7)$$

and

$$\epsilon_{rs}\frac{\partial\phi(z)}{\partial z}\bigg|_{z=t} = \epsilon_{r2}\frac{V_{g2}-V_{fb2}-\phi(t)}{t_{ox2}}. \qquad (8)$$

ϵ_{r1} and ϵ_{r2} are the relative permittivities of insulator1 and insulator2, respectively, and t_{ox1} and t_{ox2} are the corresponding thickness values of the insulators. V_{fbi} is the flatband voltage between the ith gate and the channel. Equation (6) can be solved iteratively to find $\phi(z)$. First an initial potential profile $\phi(z)$ is assumed, and then the bandstructure is calculated. This in turn provides the correction to $\phi(z)$. The process is iterated until the change in $\phi(z)$ between two successive iterations becomes less than some predefined threshold. However, every iteration requires calculation of the bandstructure. This is because the potential $\phi(z)$ adds a z dependent perturbation to the crystal potential, and thus both $E_j^{\bar{k}}$ and $\psi_j^{\bar{k}}$ are dependent on $\phi(z)$. This makes the problem computationally intensive.

To reduce the computation, the following approximation has been made. Since the potential $\phi(z)$ changes very little along z (which is shown later), as far as the change in bandstructure is concerned, it is a fair assumption that $\phi(z)$ is constant ($=\phi_c$) along z. Suppose H_0 is the original unperturbed $10N\times10N$ tight-binding Hamiltonian, and E_0 and ψ_0 are the unperturbed eigenvalues and eigenfunctions, respectively. If it is assumed that the external potential only changes the on-site energies, and does not the overlap integrals, then the perturbation ΔH can be written as

TABLE I. Mean and standard deviation values of percentage error in $\phi(z)$ and $n(z)$ for 9 and 33 monolayer thick films with $V_g=1.5$ V.

Thickness	$\phi_{\text{error}}(\%)$		$n_{\text{error}}(\%)$	
(AL)	Mean	SD	Mean	SD
9	−0.14	0.03	0.51	2.09
33	0.65	0.31	2.98	6.28

$$\Delta H = -q\phi_c I, \tag{9}$$

where I is $10N \times 10N$ diagonal unity matrix. Then,

$$H\psi_0 = (H_0 + \Delta H)\psi_0 = (E_0 - q\phi_c)\psi_0. \tag{10}$$

This essentially means that all the energy eigenvalues will be shifted by the same energy (in other words, no relative change in the energy eigenvalues), and the wave functions remain in the unperturbed states. Thus, it is sufficient to calculate the bandstructure only once, and the same $E_j^{\bar{k}}$ and $\psi_j^{\bar{k}}$ can be used through all the iterations. This reduces the total runtime by a factor of 20 to 200, depending on the number of iterations required to solve the Poisson equation.

To validate the approximation, the amount of error being incurred in the worst case (maximum gate voltage where band bending is maximum) has been examined and the results are tabulated in Table I, for both 9 and 33 monolayer thick films. The error here has been defined as $P_{error} = [(P_{approx} - P_{exact})/P_{exact}] \times 100\%$, where P_{approx} is the approximate value of parameter P and P_{exact} is the exact value of the parameter obtained from a full calculation.

In the following, to simplify the analysis, metal gates with mid-gap workfunction are assumed and the charge trapping inside the insulators is taken to be zero. This essentially means that the flatband voltages V_{fb1} and V_{fb2} are assumed to be zero. For simulation, it has been assumed that $t_{ox1}=t_{ox2}=1$ nm, $V_{g1}=V_{g2}$, and $\epsilon_{r1}=\epsilon_{r2}=3.9$.

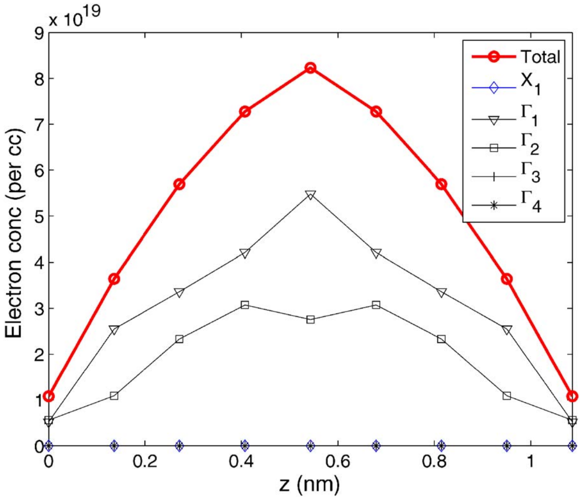

FIG. 13. (Color online) Total electron density distribution along the thickness and contribution from different subbands for a 9 atomic layer thick Si film with $V_g=1.0$ V.

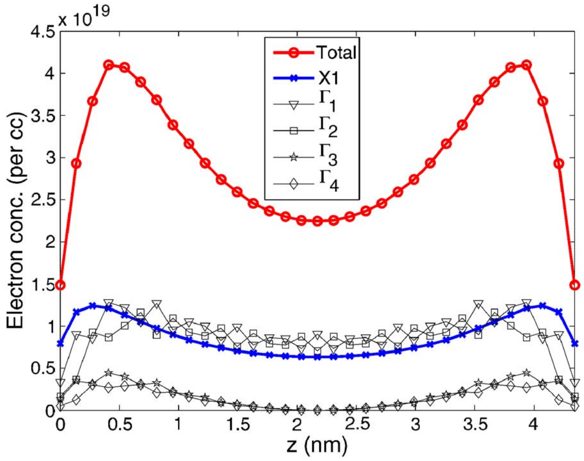

FIG. 14. (Color online) Total electron density distribution along the thickness and contribution from different subbands for a 33 atomic layer thick Si film with $V_g=1.0$ V.

A. Volume inversion

With the assumption that the bandstructure remains relatively the same under application of gate voltage, the carrier density distribution $n(z)$ can be expressed as

$$n(z) = n^0(z)e^{q\phi(z)/k_BT}, \tag{11}$$

where $n^0(z)$ is the intrinsic carrier density at z and is given by Eq. (3), and $\phi(z)$ is the potential profile obtained by solving the Eq. (6). Figures 13 and 14 show the distribution of carrier density over different subbands and the total density, for 9 and 33 monolayer thick films, respectively, with $V_{g1}=V_{g2}=1$ V. The shape of this distribution is quite different from the intrinsic carrier distribution. Also, the 9 monolayer thick film shows a higher peak carrier density compared to the 33 monolayer thick one, although the total integrated carrier concentration is higher for thicker film. This can be explained with the "*potential pinning*" effect, as discussed later. However, at any z, the fractional contribution from a subband to the total carrier density remains the same for different gate voltages. Figures 15 and 16 show the normalized carrier distribution along the depth z at different gate volt-

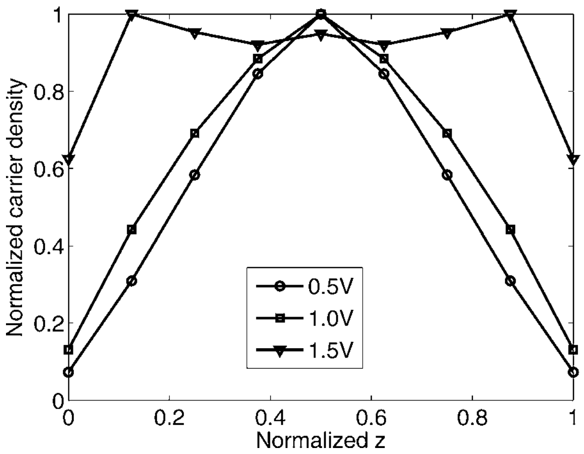

FIG. 15. Normalized total electron density distribution along the film thickness for a 9 atomic layer thick Si film with $V_g=0.5$, 1.0, and 1.5 V. Single peak is observed even at larger gate voltages.

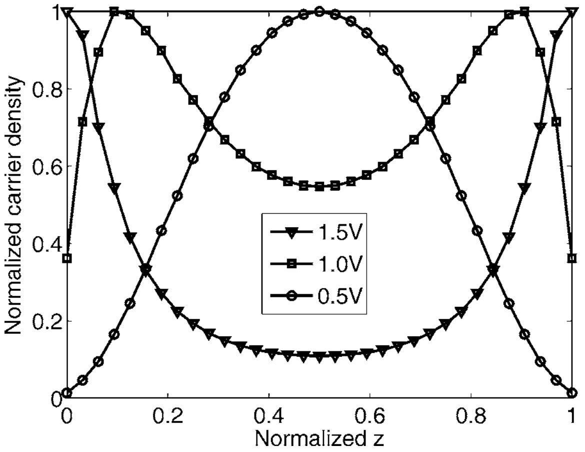

FIG. 16. Normalized total electron density distribution along the film thickness for a 33 atomic layer thick Si film with V_g=0.5, 1.0, and 1.5 V. "Double hump" characteristics are clear at higher gate voltages.

ages, for 9 and 33 monolayer thick films. The corresponding potential distribution is shown in Fig. 17. As gate voltage increases, the carriers of the "*central-peaked*" channel start spreading toward the channel-insulator interface, and beyond a particular threshold gate voltage V_{vt}, the carrier distribution will start showing two "humps" representing the separation of peaks of the carrier concentration inside the channel. V_{vt} is defined by the condition

$$\left.\frac{\partial^2 n\left(z=\frac{t}{2}\right)}{\partial z^2}\right|_{V_g=V_{vt}}=0. \qquad (12)$$

V_{vt} for a thinner film is expected to be larger than a thicker one. In other words, the carriers tend to stay closer to the center for thinner film. With the increase in gate voltage, the shifting of carrier density peaks toward the gates can be thought of as a "*carrier pulling effect*" of the gate voltage. The effect can be explained from the potential profile $\phi(z)$, which is smaller at points closer to the center of the film. It is observed from Eq. (11) that the overall carrier density profile is the product of the two terms, $n^0(z)$ and $e^{q\phi(z)/k_BT}$. $n^0(z)$ peaks at the center of the film and reduces toward the surface, whereas $e^{q\phi(z)/k_BT}$ follows the opposite trend. Thus, at a sufficiently large voltage, it is possible that the peak of the carrier density occurs at the surface. This is qualitatively the same as the classical picture, where the exponential term dominates over the "quantum mechanical" distribution of intrinsic carrier concentration. As evident from Fig. 17, the potential profile for thinner films is more uniform and is actually "pinned" at a higher value compared to the films of larger thickness. This leads to a higher peak carrier concentration in thinner films, as shown in Figs. 13 and 14.

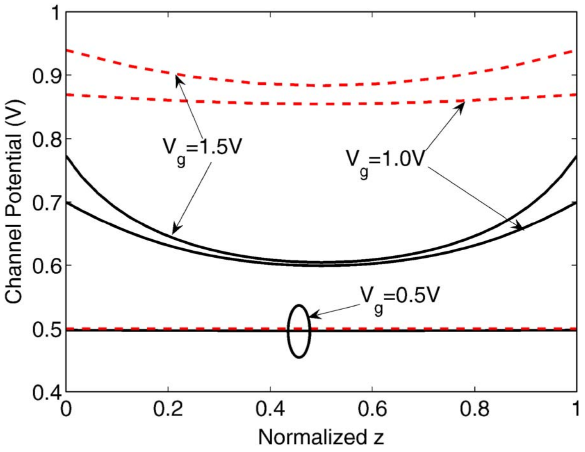

FIG. 17. (Color online) Potential distribution $\phi(z)$ along the thickness of thin Si film with three different gate voltages: 0.5, 1.0, and 1.5 V. The solid and dotted curves represent 33 and 9 monolayer thick films, respectively.

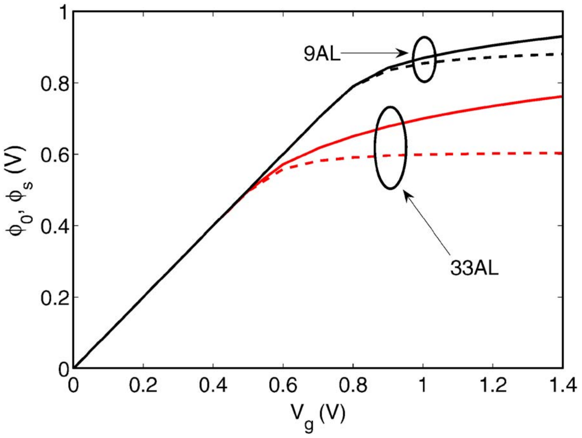

FIG. 18. (Color online) Variation of surface potential ϕ_s (solid lines) and film center potential ϕ_0 (dotted lines) with applied gate voltage V_g, for two different film thicknesses.

The above explanation becomes even more clear from Fig. 18. Initially, for small gate voltage, both the surface potential ϕ_s and film center potential ϕ_0 increase simultaneously at the same rate, and thus there will be only a single channel whose peak is at the center of the film. Beyond a certain gate voltage, ϕ_s and ϕ_0 bifurcate, and ϕ_0 saturates very quickly. However, ϕ_s keeps increasing, though at a much slower rate than earlier, causing higher carrier concentration at points closer to the surface. Finally, the single peaked channel is split and the double hump shaped channel is created. Note that, for 9 monolayer thick film, the *pinning* voltages are higher than for the 33 monolayer film.

B. Spatial channel charge distribution

The *carrier pulling effect* explained in the previous section can have an immense impact on the spatial distribution of total channel charge and hence the device performance. Consider a DGFET where the source end is grounded and $V_{ds}=V_{gs}=V_{DD}$. At any point x along the channel (with $x=0$ being taken as the source end), suppose the quasi-Fermi level is $V_{qf}(x)$. $V_{qf}(x)$ can be assumed to be independent of z. Then, the Poisson equation in Eq. (6) gets modified as[6]

$$\frac{\partial^2\phi(x,z)}{\partial z^2}=\frac{qN}{\epsilon_0\epsilon_{rs}t}\Big[\sum_j\sum_{\bar{k}}2f(E_j^{\bar{k}})|\psi_j^{\bar{k}}(\phi,z)|^2\Big]\times e^{q(\phi(x,z)-V_{qf}(x))/k_BT}, \qquad (13)$$

where all references have been made from a grounded source chemical potential. The carrier density $n(x,z)$ should now be a function of $V_{qf}(x)$ as well, which in turn depends on the

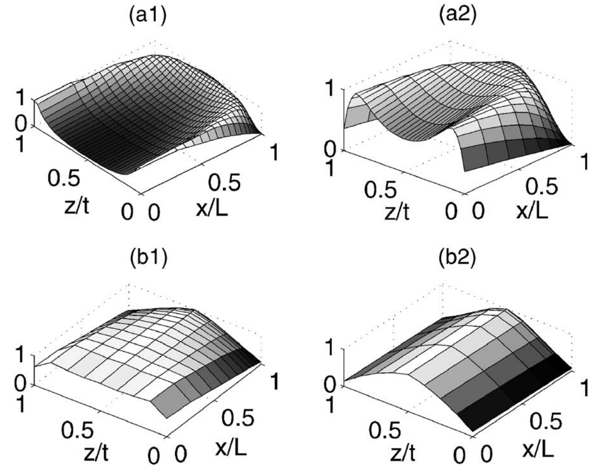

FIG. 19. Normalized carrier distribution over the whole Si channel for four different cases: (a1) 33 monolayer thick channel, $V_g=1.5$ V, $V_{DD}=1.5$ V; (a2) 33 monolayer thick channel, $V_g=1.0$ V, $V_{DD}=1.0$ V; (b1) 9 monolayer thick channel, $V_g=1.5$ V, $V_{DD}=1.5$ V; and (b2) 9 monolayer thick channel, $V_g=1.0$ V, $V_{DD}=1.0$ V.

drain voltage. Deriving the exact drain current for a nano-MOSFET needs proper attention on the carrier transport model. However, to get a quantitative estimate, a long channel device ($L=1$ μm, $W=1$ μm) with a constant mobility has been assumed. The drain current and $V_{qf}(x)$ have been calculated using a similar procedure as in Ref. 6 by self-consistently solving Eq. (13) with the drain current continuity equation. The extracted normalized carrier concentration $n'(x,z)$ is plotted over the whole channel region in Fig. 19 for different cases. At any $x=x_0$, $n'(x_0,z)$ has been defined as

$$n'(x_0,z)=\frac{n(x_0,z)}{\mathrm{MAX}_z\{n(x_0,z)\}}, \tag{14}$$

where $\mathrm{MAX}_z\{.\}$ represents the maximum value of $\{.\}$ over z. The normalization is done in such a way which clearly shows the spatial shape of carrier distribution at different x's. It is observed that at the source end ($x=0$), due to larger potential difference between the gate and the channel, there clearly exist two distinct carrier density peaks. However, as one moves toward the drain end, the potential difference between gate and channel reduces, and the two distinct peaks merge together producing a single center-peaked channel. Also, the magnitude of the total carrier concentration reduces near the drain end. In other words, the carriers stay closer to the surface near the source end whereas, near the drain end, the carriers stay closer to the center of the channel. Thus, closer to the source end, one expects higher mobility degradation due to vertical field effect and surface scattering effect compared to the drain end. Similar effects are true for gate leakage and gate capacitance, which can no longer be assumed to be uniform along the channel. It is evident from Fig. 19 that this effect is more pronounced in the thicker channel devices and at higher operating voltages. If the channel is thin enough, as is the case of (b2) in Fig. 19, it is possible to have a single peaked channel all over the device.

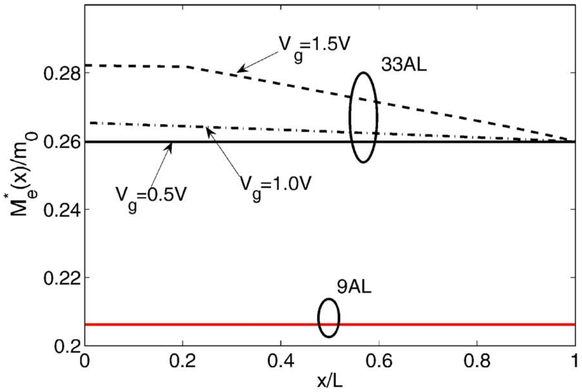

FIG. 20. (Color online) Variation of *average effective mass* $M_e^*(x)$ of carriers with channel along $\langle 100\rangle$ direction for different channel thickness values and different gate voltages V_g with $V_{DD}=V_g$.

C. Evolution of effective mass along DGFET channel

In Sec. III, the variation of $\langle 100\rangle$ $M^*(z)$ along the thickness for a thin film Si has been discussed in detail. Now, in a DGFET channel, the potential difference between gate and channel changes from the source end to the drain end. Thus the total number of carriers at different subbands also changes along the channel. Keeping this in mind, one can define an "*average effective mass*," $M_e^*(x)$,

$$M_e^*(x)=\frac{\int_0^t n(x,z)dz}{\int_0^t \frac{n(x,z)}{M^*(z)}dz}, \tag{15}$$

which is basically a harmonic average over the carriers along the thickness at a particular position x along the channel length. Physically, this indicates the "average" effective mass of an electron located at distance x from the source along the channel. Strictly speaking, Eq. (15) is valid only under the assumption that the vertical field is fairly constant and each electron suffers the same scattering rate. Although this is not a very good approximation, it gives an idea of how the channel charge distribution can affect the spatial distribution of carrier effective mass. It is observed from Fig. 20 that for very thin channel (e.g., 9 monolayer), $M_e^*(x)$ hardly varies with x or V_g. However, for higher channel thickness, a gradual decrease in $M_e^*(x)$ is observed from the source end to the drain end, and the effect is more prominent for higher gate voltages.

D. Channel capacitance

Qualitatively, the charge distribution in a quantum analysis has two major differences compared to the classical analysis: (1) The total charge in the channel reduces and (2) the charge distribution peak shifts from the surface toward the center of the film. The extent of the shift depends on the applied gate voltage. Both these effects cause a change in the total channel capacitance.[5] The channel capacitance per unit volume $C_{si}(z)$ at a depth z can be defined as the rate of change of charge per unit volume with respect to the potential at that point. Mathematically,

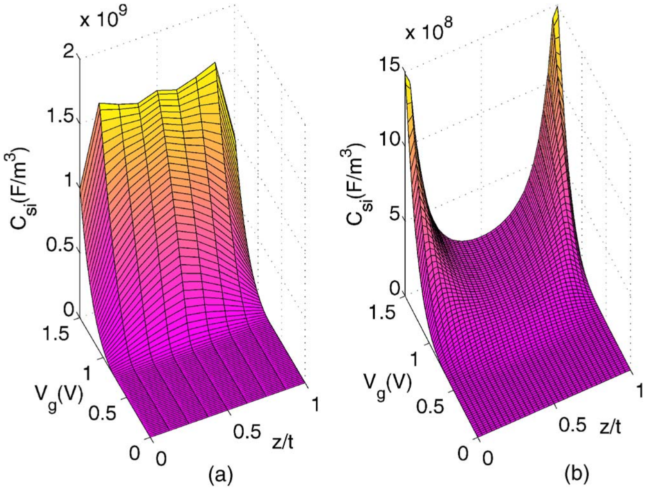

FIG. 21. (Color online) C_{si} as a function of V_g and depth z along thickness of channel for (a) 9 monolayer thick channel and (b) 33 monolayer thick channel.

$$C_{si}(z) = \frac{\partial Q_{si}(z)}{\partial \phi(z)}, \qquad (16)$$

where $Q_{si}(z)$ is given by

$$Q_{si}(z) = \frac{qN}{t}\left[\sum_{j}\sum_{\bar{k}} 2f(E_j^{\bar{k}})|\psi_j^{\bar{k}}(\phi,z)|^2\right] e^{q\phi(z)/k_BT}. \qquad (17)$$

Figure 21 shows the variation of channel capacitance with z and V_g. One should note that the position $z=z_{\max}$ inside the film, where $C_{si}(z)$ is maximum, varies with gate voltage and, as the gate voltage increases, $z_{\max}$ shifts toward the surface.

V. CONCLUSION

A detailed analysis of UTB DGFET has been performed in this work. The channel material has been chosen to be Si, but the analysis and methodology can be readily extended to other promising channel materials as well. Ultra-thin film of Si has been shown to have larger (and direct) band gap, compared to bulk. It has also been shown that the intrinsic carrier concentration is not only less compared to bulk, but also has a distribution over the channel thickness, peaking at the center. The contributions of different subbands from the different valleys to both intrinsic carrier concentration as well as effective mass have been analyzed. The spatial variation of distributed $\langle 100\rangle$ effective mass along the thickness has been studied. It has also been shown that along the $\langle 100\rangle$ direction, parabolic effective mass concept is valid until an electronic energy of ~0.5 eV from the corresponding subband minima in all the relevant valleys. A detailed analysis of volume inversion has been performed with the help of the self-consistent solution of coupled Poisson-Schrödinger equations. Channel charge distribution in a DGFET has been predicted using the concept of *carrier pulling effect* of gate voltage. The effects of channel charge distribution on effective mass and channel capacitance have been analyzed.

ACKNOWLEDGMENTS

The authors would like to acknowledge the support from Ministry of Communication and Information Technology (MCIT), Govt. of India, under the Center of Excellence in Nanotechnologies project. In addition, the support from Department of Science and Technology (DST), Govt. of India, is also acknowledged. The authors thank the SERC Department at IISc for providing high performance computational resources.

[1] F. Balestra, S. Cristoloveanu, M. Benachir, J. Brini, and T. Elewa, IEEE Electron Device Lett. **8**, 410 (1987).
[2] J. G. Fossum, L. Ge, and M. H. Chiang, IEEE Trans. Electron Devices **49**, 808 (2002).
[3] T. Ernst, S. Cristoloveanu, G. Ghibaudo, T. Ouisse, S. Horiguchi, Y. Ono, Y. Takahashi, and K. Murase, IEEE Trans. Electron Devices **50**, 830 (2003).
[4] Y. Taur, IEEE Electron Device Lett. **21**, 245 (2000).
[5] Y. Taur, IEEE Trans. Electron Devices **48**, 2861 (2001).
[6] Y. Taur, X. Liang, W. Wang, and H. Lu, IEEE Electron Device Lett. **25**, 107 (2004).
[7] T. Ouisse, J. Appl. Phys. **76**(10), 5989 (1994).
[8] F. Gamiz and M. V. Fischetti, J. Appl. Phys. **89**(10), 5478 (2001).
[9] L. Ge and J. G. Fossum, IEEE Trans. Electron Devices **49**, 287 (2002).
[10] F. Stern, Phys. Rev. B **5**, 4891 (1972).
[11] J. C. Slater and G. F. Koster, Phys. Rev. **94**, 1498 (1954).
[12] D. J. Chadi and M. L. Cohen, Phys. Status Solidi B **68**, 405 (1975).
[13] P. Vogl, H. P. Hjalmarso, and J. D. Dow, J. Phys. Chem. Solids **44**, 365 (1983).
[14] J. M. Jancu, R. Scholz, F. Beltram, and F. Bassani, Phys. Rev. B **57**, 6493 (1998).
[15] T. B. Boykin, G. Klimeck, R. C. Bowen, and F. Oyafuso, Phys. Rev. B **66**, 125207 (2002).
[16] T. B. Boykin, G. Klimeck, and F. Oyafuso, Phys. Rev. B **69**, 115201 (2004).
[17] S. Lee, F. Oyafuso, P. von Allmen, and G. Klimeck, Phys. Rev. B **69**, 045316 (2004).
[18] A. Rahman, G. Klimeck, and M. Lundstrom, IEDM Tech., p. 601, 2005.
[19] S. E. Laux, IEDM Tech., p. 135, 2004.
[20] A. Pethe, T. Krishnamohan, D. Kim, S. Oh, P. Wong, Y. Nishi, and K. C. Saraswat, IEDM Tech., p. 605, 2005.
[21] J. van der Steen, D. Esseni, P. Palestri, L. Selmi, and R. Hueting, IEEE Trans. Electron Devices **54**, 1843 (2007).
[22] D. Vasileska, D. K. Schroder, and D. K. Ferry, IEEE Trans. Electron Devices **44**, 584 (1997).
[23] L. Ge, F. Gamiz, G. O. Workman, and S. Veeraraghavan, IEEE Trans. Electron Devices **53**, 753 (2006).
[24] O. Moldovan, D. Jimenez, J. R. Guitart, F. A. Chaves, and B. Iniguez, IEEE Trans. Electron Devices **54**, 1718 (2007).